ROYAL SOCIETY
OF CHEMISTRY

PAPER

Check for updates

New nanostructured, ion-conductive, bent-core liquid crystals containing lithium and sodium salts as soft electrolyte candidates

Carlota Auria-Soro, [ID] [ab] Nuria Cruz-Navarro, [ab] César L. Folcia, [ID] [c]
Isabel Sobrados, [ID] [d] Amin Sharifi Haddad, [ID] [e] Alfonso Martínez-Felipe [ID] *[e]
and M. Blanca Ros [ID] *[ab]

Two new tetraethylene glycol (TEG)-containing bent-core molecules are revealed as suitable, versatile supramolecular building blocks to form liquid crystalline phases and organogels in novel structured soft electrolytes. New amphiphilic bent-core molecules [**TEG-Bx-10-14**], composed of a short polar TEG-segment capping and well-defined bent-core, mesogenic-like structures, and a set of their [1/1] complexes with TfO^- and Tf_2N^-/lithium and sodium salts [**MA-TEG-Bx-10-14**], are investigated for the first time. FT-IR, ^{13}C CP-MAS-NMR and ^1H MAS-NMR studies at variable temperatures indicate the selective complexation of cations in the TEG regions. Although new bent-core molecular designs [**TEG-10-Bx-14**] do not exhibit liquid crystal order, most of their complexes [**MA-TEG-10-Bx-14**] stabilize an attractive number of bent-core lamellar mesophases (SmCP, HNF-like, USmCP and Col_{ob}). Diffusion coefficients (D) of lithium, favoured by the liquid crystal phase transition, are estimated by solid state NMR spectroscopy. The direct current values of $\sigma_{dc} \sim 10^{-4}$ S cm^{-1} in the mid-high frequency range were found using dielectric spectroscopy, highlighting the potential of bent-core building blocks as organic and nanostructured soft electrolytes containing both lithium and sodium cations, whose ionic conductivities can be optimised through composition tuning and annealing.

1. Introduction

Advanced materials with tailor-made functionalities will play a vital role in accelerating energy transition and the 4th industrial revolution by offering sustainable solutions to some of the most urgent challenges in today's World.[1] Thus, research on materials with high capacity density and improved safety features is crucial to increase productivity in the sectors that require modernization and innovation in different areas of specialization. Electrochemical energy storage systems (EESS) are particularly attractive to promote energy integration, and among them, ion-batteries and supercapacitors can boost the use of renewable energies in electric transport, mobile electronic devices and the aerospace sector. In this context, solid (or quasi-solid) state electrolyte (SSE) devices hold promise as

contenders in portable energy applications[2–6] due to their non-flammable nature, low weight, absence of fluids, and resistance to dendrite formation. Despite these promising features, some obstacles must be overcome prior to their widespread implementation, such as limited conductivity, high cost, poor electrolyte–electrode interface interactions, and processing challenges.[7–10]

Liquid crystal electrolytes (LCEs),[11–18] including ionic liquid crystals,[19–24] have stimulated huge interest in the search for novel solvent-free electrolytes. On the one hand, they provide groups for ion binding, and on the other hand, their structural order at the nanometric scale facilitates pathways for ionic diffusion and mechanical resistance to the material. Additionally, the fluid nature of the mesophases can promote not only local charge mobility but also mild processing conditions. These properties are strongly determined by molecular assembly, making the molecular design of novel LCEs paramount for yielding functional nanostructures useful in electrochemical processes. Inspired by the conductivity of poly(ethylene oxide)-based polymers,[17,18,25–30] a number of ethylene oxide-decorated mesogens have been successfully proposed as non-ionic electrolytes,[17,18,31,32] providing 1D, 2D and 3D nanostructured classic columnar, smectic and discontinuous cubic mesophases, respectively, whose orientation can be manipulated to some extent.[11–18,31,32] Recently, ethylene oxide

[a]Instituto de Nanociencia y Materiales de Aragón (INMA), CSIC-Universidad de Zaragoza, 50009 Zaragoza, Spain

[b]Departamento de Química Orgánica, Facultad de Ciencias, Universidad de Zaragoza, 50009 Zaragoza, Spain

[c]Department of Physics, Faculty of Science and Technology, UPV/EHU, E-48080 Bilbao, Spain

[d]Instituto de Ciencia de Materiales de Madrid, Consejo Superior de Investigaciones Científicas (CSIC), E-28049 Madrid, Spain

[e]Chemical Processes and Materials Research Group, Just Transition Lab, Centre for Energy Transition, University of Aberdeen, Aberdeen, AB24 3UE, Scotland, UK

moieties have been postulated to promote novel bent-core liquid crystal (BCLC) phases by complexation with lithium ions, even from non-mesogenic bent-core molecules.[33,34] Thus, ionic conductivity can serve as a cornerstone for other features of BCLC, such as their ferro-, piezo-, and pyro-electric, nonlinear optical, fluorescence, photoconductivity or magnetic responses,[35–39] opening new venues for nanostructured soft electrolytes.

With the aim of developing TEG-based advanced electrolytes, herein, we report the synthesis, liquid crystalline properties and functionality of a new family of bent-core molecules, labelled as **TEG-10-Bx-14** (Scheme 1) and their complexes with various alkali salts. We synthesised new materials based on ethylene oxide (EO)/alkali cation tandems by mixing the TEG-decorated compounds with a variety of different alkali salts [MA] in 1/1 molar ratios, yielding complexes labelled as **MA-TEG-10-Bx-14** (Scheme 1). The short TEG-chain is again selected to induce nanophase segregation and to confer hydrophilicity but mainly to drive the transport of alkali cations. In particular, we conducted a systematic study in terms of the bent-core structure, the cation ($M^+ = Li^+$ or Na^+) and anion ($A^- = CF_3SO_3^-$, *aka* TfO^-, or $(CF_3SO_2)N^-$, *aka* Tf_2N^-) serving as an essential component of electrolytes.[40] From an electrolyte-design perspective, TfO^- and Tf_2N^- were chosen as large, weakly coordinating anions that dissociate efficiently in ether-rich polymer and gel electrolytes, thereby increasing the concentration of mobile ions while providing high thermal and electrochemical stability.[6,25,41,42] In Li-based systems, LiTfO and LiTf$_2$N are benchmark salts in PEO-based solid polymer electrolytes,[6,25] while their sodium NaTfO and NaTf$_2$N analogues play a comparable role in state-of-the-art Na-ion electrolytes, where anion-dominated solvation and interphase chemistry critically govern performance.[41,42]

This work pursues a progression from our previously reported bent-core materials (Scheme 1),[33] in which the TEG-segment was directly grafted to the bent-core. We now present molecular designs with a better-defined "classical" bent-core structure to guide their supramolecular nanostructures. In these new compounds, the promesogenic bent-core moiety is surrounded by two long aliphatic chains on both sides, namely a 14 carbon-atom as a terminal tail and a 10 carbon-atom as a spacer disconnecting the bent-core and the TEG-motive. Two alternative aromatic bent-cores (Bx) are used in the current study: one based on a common ester linking group (B1) largely used to stabilize broad ranges of lamellar bent-core mesophases (yielding compound **TEG-10-B1-14**),[43–48] and a biphenyl-based one (Bi) inspired by the trend of biphenyl lateral cores to promote singular helical nanofilament phases (HNF)[43–52] (yielding compound **TEG-10-Bi-14**). Distinctively, we explore sodium ion (Na^+)-based hybrid materials[8] as alternatives to lithium ion (Li^+)-based materials. Sodium shows an appropriate redox potential, it is cheaper, abundant and well distributed in the Earth's crust and can avoid long-term concerns about safety and critical raw materials. Ultimately, we assess the potential of our bent-core compounds to form supramolecular gels, taking advantage of their amphiphilic character. We envisage that both series, **TEG-10-Bx-14** and **MA-TEG-10-Bx-14**, are suitable building blocks to yield highly demanded nanostructured organogels by their self-assembly into fibrillar morphologies, comparable to the molecular arrangement in the mesophase, also providing alternative routes to obtain soft electrolytes.

2. Experimental part

2.1. Synthesis and characterisation of EO-based bent-core amphiphiles

These novel EO-bent-core amphiphiles, **TEG-10-Bx-14** compounds and the supramolecular complexes, **MA-TEG-10-Bx-14**, were synthesised using a convergent approach, following the method described in the SI (Schemes S1–S6).

To obtain the **TEG-10-Bx-14** compounds, the initial step involved the synthesis of the bent-structure of 4′-benzyloxy-biphenyl-3-ol through a Pd(0)-catalyzed Suzuki cross-coupling reaction. Then, Steglich esterifications with phenolic intermediates were used to obtain the common compound, including the 10-carbon spacer. Subsequently, two carboxylic acids bearing different X-linkers were prepared according to previously described methods.[33,34,53–57] After appropriate catalytic hydrogenation, esterification and elimination steps, bent-core-based carboxylic acids were formed, which finally allowed the incorporation of the TEG moiety. The chemical structures of the bent-core compounds **TEG-10-B1-14** and **TEG-10-Bi-14** were assessed using ^{1}H-NMR spectroscopy, ^{13}C-NMR spectroscopy, FT-IR spectroscopy, mass spectrometry and elemental analysis. Detailed descriptions of the synthetic scheme, procedures and structural characterization of the compounds are provided in the SI.

2.2. Preparation of alkali metal complexes

The alkali metal complexes of the **TEG-10-Bx-14** compounds were prepared by the slow evaporation of THF solutions
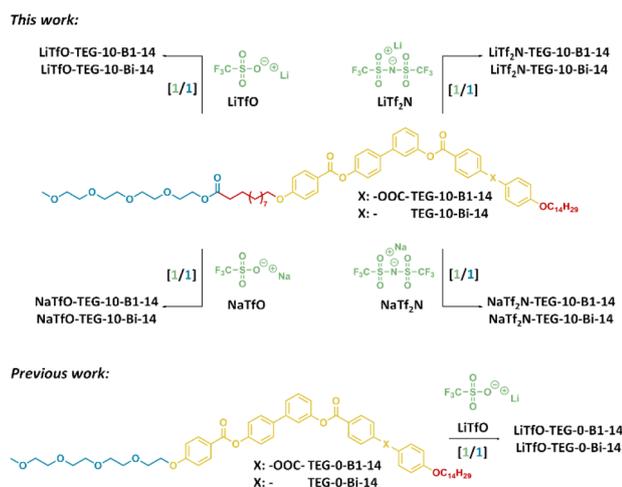
Scheme 1 Chemical structures and identification of the new tetra-ethylene oxide (TEG)-based bent-core compounds and their [1/1] cation/MA-TEG-10-Bx-14 complexes; the previously reported **TEG-0-Bx-14** analogues are shown below for comparison.[33]

This journal is © The Royal Society of Chemistry 2026

J. Mater. Chem. A, 2026, **14**, 11294–11309 | **11295**

containing appropriate amounts of the bent-core amphiphiles and the corresponding salts. This process resulted in an average of four EO repetitive units per one ionic salt. ^{1}H-NMR and FT-IR spectroscopy (see Fig. S3 and S6) were used to study all complexes and to confirm the location of the ion species preferentially bonded to the TEG segments of the bent-core molecules.

^{1}H-NMR studies in solution show that, in general, the complexes exhibit downfield shifting of the $-CH_2-O-$ signals associated with ion/EO interactions, while the signals corresponding to both the hydrogen atoms of the aromatic rings and those from the inner and terminal aliphatic chains remain unchanged (see Fig. S3).

The FT-IR spectra at room temperature ($T = 25$ °C, Fig. S6) provide substantial evidence of coordination interactions between the EO-chains and the alkali ions. According to our previous study, selective complexation of the LiTfO ions in the EO region was confirmed in bulk by the appearance of new infrared band contributions (1310, 1040 and 640 cm^{-1}) and broadening of the C–O–C stretching bands (1254, 1206, 1168, 1137 and 1067 cm^{-1}).[58–61] However, it is noteworthy that the shift associated with NaTfO was less pronounced, which is consistent with the results obtained from ^{1}H-NMR studies. Furthermore, MTf$_2$N-doped materials showed new prominent peaks near 1354 (ν_{as}) and 1140 (ν_s) cm^{-1} on complexation, which are related to the asymmetric and symmetric stretching vibrations of $-SO_2$, respectively. Simultaneously, an increase in the 1200 cm^{-1} peak is observed, which is related to the asymmetric vibrations (ν_{as}) of the $-CF_3$ groups present. New signals were also identified at 1065 cm^{-1} (ν_{as}(S–N–S)), 950 cm^{-1}, ν(S–N) and ν(C–S) and 620 cm^{-1} (δ(S–N)). All these results confirm the formation of the LiTf$_2$N and NaTf$_2$N complexes.

2.3. Preparation of physical gels

The gelation behaviour of both pure and complexed materials was investigated using two solvents, 1-octanol and n-dodecane, which have different polarities and chemical natures. To this end, mixtures containing 1 wt% of the bent-core component and selected solvents were prepared, heated to approximately 5 °C below the boiling point of the solvents and then allowed to cool to room temperature. To determine whether the materials induce stable physical gels, a *vial inversion test* was subsequently conducted.

2.4. Dielectric and conductivity measurements

The dielectric response and ionic conductivity of the materials were assessed in transparent cells between the parallel electrodes. A few milligrams of the samples were introduced in the melt state by capillary action inside indium tin oxide (ITO) cells (SG100A080μG180, Instec) containing polyimide coatings to yield anti-parallel alignments with 1° to 3° pre-tilted angles. Cells have active areas of $A = 25$ mm^2 with 100 Ω resistance and $v = 3.2$ μm thickness and the cell capacitance is then calculated as follows:

$$C_0 = \varepsilon_0 \frac{A}{v} = 6.91719 \times 10^{-11} \text{ F},$$

where $\varepsilon_0 = 8.854 \times 10^{-12}$ Fm^{-1} is the dielectric permittivity of vacuum.

The phase behaviour of the materials inside the ITO devices was assessed by polarised optical microscopy (POM) using an Olympus BX53 microscope with a DP23 camera sensor, with the temperature controlled by a Linkam THMS 600 heating stage and TMS 91 control unit (± 0.1 K).

The dielectric and conductivity responses of the materials in the cells were studied by complex impedance spectroscopy in terms of their complex dielectric permittivity:

$$\varepsilon^* = \varepsilon' - i\varepsilon'', \tag{1}$$

where ε' is the dielectric elastic constant, ε'' is the loss factor and i is the complex unity. The complex conductivity is defined as follows:

$$\sigma^* = \sigma' - i\sigma'', \tag{2}$$

where σ' and σ'' are the real and imaginary conductivity components, respectively. The dielectric permittivity and conductivity are related by

$$\sigma^* = i\omega\varepsilon_0\varepsilon^*, \tag{3}$$

where ω is the angular frequency of the alternating electrical field, rad s^{-1}.

The ITO cells were connected to a Solartron Modulab XM frequency response analyser (FRA) using a Linkam TMS 91 hot stage for temperature control (± 0.1 °C). The dielectric measurements consisted of isothermal frequency sweeps between 106 Hz and 0.1 Hz, with $V_{rms} = 1000$ mV amplitude alternating electric fields and the majority were taken in the absence of bias direct current electric fields ($V_{bias} = 0$ V). Experiments were carried out by cooling from the isotropic phase to room temperature in 2 °C isothermal steps, allowing for thermal equilibrium before measurement.

2.5. Spectroscopic measurements in bulk

2.5.1. FT-IR studies. FT-IR spectra at room and variable temperatures were acquired to determine short-range interactions involving different molecular segments using a Bruker Vertex 70 spectrometer with 4 cm^{-1} resolutions in the 4000–600 cm^{-1} range, as the average of 64 scans and analysed with OPUS software using a Mettler FP80 HT hot stage for temperature control. Measurements were taken in transmission mode with samples sandwiched between KBr discs, at a heating rate of 5 °C min^{-1}.

2.5.2. NMR measurements. ^{13}C CP-MAS-NMR and ^{1}H MAS-NMR spectra of the **LiTfO-TEG-10-B1-14** complex were recorded using a Bruker Avance 400 spectrometer as a representative example, with an external magnetic field of 9.4 tesla. Powder samples were packed in zirconia rotors. Monodimensional spectra were obtained at room temperature, while the samples were spun at 10 kHz around the magic angle (54°44′ with

11296 | *J. Mater. Chem. A*, 2026, **14**, 11294–11309

This journal is © The Royal Society of Chemistry 2026

respect to the magnetic field) with a standard cross-polarization pulse sequence. Spectrometer frequencies were set to 100.62 and 400.13 MHz for ^{13}C and ^{1}H, respectively. For quantitative purposes, the contact time was analysed in the CP experiments. A contact time of 2 ms and a period between successive accumulations of 5 s were used to minimize the saturation effects of 400 scans. In the case of ^{1}H spectra, the number of accumulations was 40 and the time between accumulations was 5 s. Chemical shifts of the ^{1}H and ^{13}C signals indicated those of the TMS reference. ^{7}Li MAS NMR spectra were recorded at 155.51 MHz, with a pulse length of 3.25 µs, 5 s of recycled delay and 96 accumulations. Chemical shifts were referenced to a 4 M LiCl solution.

2.5.3. Pulse field gradient. Self-diffusion coefficients were determined by applying the PFG technique with a Bruker diffusion probe head Diff60 using a $\pi/2$ irradiation ^{7}Li pulse length of 8.5 µs. In these experiments, the stimulated echo $\pi/2$–t_1–$\pi/2$–t_2–$\pi/2$ sequence was used in which two field gradient pulses of δ width and g intensity were applied between the first two $\pi/2$ pulses and after the third $\pi/2$ radio frequency pulse. A spoiler gradient was used between the second and third $\pi/2$ pulses. From the echo-signal attenuation induced by the increment of exponent parameters, self-diffusion coefficients (D_{PFG}) were deduced using the Stejskal and Tanner expression deduced for free diffusion:

$$\frac{A(2t_1 + t_2)}{A_0(2t_1 + t_2)} = e^{\left(-\gamma^2 g^2 \delta^2 \left(\Delta - \frac{\delta}{3}\right) D_{PFG}\right)} = e^{(-bD_{PFG})}, \qquad (4)$$

where A and A_0 denote echo signal intensity at $(2t_1 + t_2)$ with and without field gradient pulses, respectively, γ is the nuclear gyro magnetic ratio and Δ is the diffusion time used in the experiments. These experiments were performed keeping δ and D_{PFG} values constant and increasing the gradient pulse intensity g from 0 to 1200 G·cm^{-1}. Similar determinations can be performed by fixing g and D_{PFG} and increasing δ values; however, in this case, the short-pulse approximation is difficult to comply with. The range of DPFG values, explored with the PFG NMR technique, ranges from 10^{-8} to 10^{-13} m^2 s^{-1}. In the present work, δ values were fixed at 2 ms, but Δ values were 150 and 100 ms for the first and second thermal treatments, respectively. In PFG measurements, relaxation T_2 values corrected from B_0 inhomogeneity must be longer than 2 ms and the repetition rate must be five times T_1 values (5×10^{-2} to 1 s). Both requirements were compiled in PFG experiments performed in the temperature range of 300–425 K. Diffusion coefficients were analysed *vs.* inverse temperature to deduce activation energies. Previously, the gradient was calibrated using a LiCl 4 M aqueous solution and a value of the diffusion coefficient equal to $6.8\ 10^{-10}$ m^2 s^{-1}. The linear $\ln[A(2t_1 + t_2)/A_0(2t_1 + t_2)]$ dependences on b ($\gamma^2 g^2 \delta^2 (\Delta - \delta/3)$) values were used to determine the diffusion coefficients.

3. Results and discussion

3.1. Short-range interactions

Selective complexation of the Li$^+$ and Na$^+$ ions in the TEG region was confirmed by the appearance of new IR contributions attributed to the TfO$^-$ and Tf$_2$N$^-$ ions (Fig. S7). When cooling from the isotropic liquid to the crystal phase, the main bands attributed to the EO moieties became broader and appeared to split into different contributions. Interestingly, this effect was not observed in our previous studies on bent-core compounds with the TEG-moiety directly grafted to the aromatic-core.[33,34] This suggests the presence of new dipole interactions between the TEG units and the ions typical of cooperative molecular systems, which could be attributed to the –COO– connecting group within the terminal tail. Nevertheless, no significant shift in these signals with temperature was observed, indicating that –CH$_2$–O–CH$_2$– moieties maintain the same conformation upon cooling from the isotropic liquid phase.

^{13}C CP-MAS-NMR spectra carried out for **TEG-10-B1-14**-based samples show fine and well-resolved signals in various ^{13}C chemical shift ranges, associated with materials with good crystallinity. Pristine and Li-based complexes present small differences, with the most notable being the decrease in signal intensity in the range of 75–60 ppm in the lithiated compound (Fig. S4). This may indicate, as expected, that carbons 1–9 (see Fig. S1) at the TEG tail are the most affected by the incorporation of the ion. The good resolution of the components at room temperature is lost when the sample is heated to 120 °C, reaching the isotropic liquid.

The ^{1}H MAS-NMR spectra of **TEG-10-B1-14** and **LiTfO-TEG-10-B1-14** (Fig. S5) display wide profiles resulting from a sum of components. Table 1 summarizes the deconvolutions carried out on the spectra of these two samples at room temperature and 120 °C (isotropic liquid), which can be compared with the assignments of the ^{1}H NMR spectra in solution (see Fig. S1). The deconvolution of the signals corresponding to liquid samples and crystalline solids presents narrow peaks (with small Full Width Half Maximum values, FWHM). In solids, the lines are wider, typical of amorphous materials with more heterogeneous molecular environments. From the data in Table 1, the proton zone corresponding to the –CH$_2$–O–CH$_2$– groups is identified as the most affected by the introduction of lithium.

The ^{7}Li MAS NMR spectrum was satisfactorily fitted to two signals of different line-widths (0.3 and 2.3 ppm) (Fig. S5B) at the same isotropic chemical shift (−0.93 ppm). The relative intensity of both components is close to 3 : 1. The most abundant narrow ^{7}Li component was ascribed to the fast lithium species with average dipolar and quadrupolar interactions on the NMR timescale; this

3.2. Liquid crystal behaviour

The evaluation of the liquid-crystalline properties of the ethylene oxide bent-core amphiphiles and their complexes was conducted using a combination of analytical techniques with characteristics described in the SI.

3.2.1 Thermal studies. Thermogravimetric analysis (TGA) revealed that all materials under study exhibit good thermal stability, with decomposition associated with a weight loss of 5% occurring at temperatures above $T_{5\%} > 230$ °C, in all cases above the respective transition to the isotropic liquids (Table 2). POM images and differential scanning calorimetry (DSC)

This journal is © The Royal Society of Chemistry 2026

J. Mater. Chem. A, 2026, **14**, 11294–11309 | **11297**

Table 1 Deconvolution of the ^{1}H MAS NMR spectra of the **TEG-10-B1-14** compound and **LiTfO-TEG-10-B1-14** complex[a]

		H–Ar		–CH$_2$–O–CH$_2$–			–CH$_2$–			
TEG-10-B1-14 (rt)	δ (ppm)	9.05	7.30	5.78	3.84	3.67	2.89	1.54	0.40	−1.10
	FWHM	3.00	3.00	3.01	0.37	0.31	0.65	1.30	0.57	3.50
	%	3.46	11.78	15.27	20.64	29.08	7.49	9.00	0.81	2.48
LiTfO-TEG-10-B1-14 (rt)	δ (ppm)	7.48	6.42	5.39	4.21	3.88	2.66	2.02	1.32	0.63
	FWHM	1.57	1.69	1.17	0.33	0.53	0.92	0.38	0.59	1.34
	%	4.40	7.62	4.84	7.15	49.01	10.07	8.51	3.89	4.51
LiTfO-TEG-10-B1-14 (120 °C)	δ (ppm)	7.43	6.43	5.42	—	3.75	2.44	1.91	1.28	0.60
	FWHM	1.57	1.69	1.17	—	0.54	0.92	0.46	0.59	1.80
	%	3.94	6.31	3.95	—	56.04	6.91	8.30	3.97	10.77

[a] FWHM: full width half maximum (width at half height that has a peak) fraction of charge carriers is what causes long-distance motions. Smaller prominent components can be associated with lithium ions in less mobile positions.

Table 2 Phase transition temperatures, liquid-crystalline behaviour and degradation temperatures of the TEG-based bent-core compounds and alkali-doped materials

Compound	Phase transitions °C [kJ mol^{-1}][a]	T_5% °C[b]
TEG-10-B1-14	Cr 69 [63.7][c] I	365
	I 66 [68.4] Cr	
TEG-10-Bi-14	Cr 98 [60.9] I	321
	I 93 [71.7] Cr	
LiTfO-TEG-10-B1-14	Cr 83 [20.5][c] SmCP 107[d] [13.9] I	284
	I 105 [18.3][e,f] SmCP 76 [20.7] Cr	
LiTfO-TEG-10-Bi-14	Cr 117[d] [39.7][g] I	314
	I 117[d] [10.6] HNF-like 113 [35.9] Cr	
LiTf$_2$N-TEG-10-B1-14	Cr$_1$/Cr$_2$ 68 [25.7][c] SmCP 85 [10.4] I	230
	I 84[d] [11.5] SmCP 75 [1.4][h] HNF-like 65 [22.6] Cr	
LiTf$_2$N-TEG-10-Bi-14	Cr 105[d] [38.3][c] I	256
	I 102 [37.7][i] HNF-like – Cr	
NaTfO-TEG-10-B1-14	Cr 65 [41.8] I[j]	252
NaTfO-TEG-10-Bi-14	Cr 105 [43.2] I[j]	260
NaTf$_2$N-TEG-10-B1-14	Cr 83[d] [38.1][c] I	323
	I 82 [16.7] USmCP 64 [16.9] Cr	
NaTf$_2$N-TEG-10-Bi-14	Cr 97 [32.4][c] I	329
	I 96 [34.1][i] Col$_{ob}$ – Cr	

[a] Data determined by DSC. Temperatures at the onset of the peaks from the second heating and cooling cycles at a scanning rate of 5 °C min^{-1}. Cr: crystal phase, SmCP: smectic C polar mesophase, HNF-like mesophase, morphological variant of helical nanofilament mesophase not fully identified, USmCP: undulated smectic C polar mesophase, Col$_{ob}$: columnar oblique mesophase, I: isotropic liquid. [b] Data determined by TGA at 5% mass loss temperature. [c] Combined enthalpies of several peaks. [d] Temperature at the peak. [e] Combined enthalpies of several peaks, including a mesophase–mesophase transition. [f] Coexistence of two mesophases detected by POM. [g] Combined enthalpies of several peaks, including a crystal–mesophase transition. [h] Transition assigned based on DSC and POM studies. [i] Combined enthalpies of a broad peak, including a mesophase–crystal transition. [j] Transition detected by DSC, but non-homogenous samples are observed by POM.

thermograms showed that none of the **TEG-10-Bx-14** compounds formed liquid crystalline self-assemblies. In contrast, complexation induces liquid crystallinity, either during heating or just on cooling (Table 2, Fig. S8 and S9).

POM observations reveal that most **MA-TEG-10-Bx-14** complexes form homogenous domains that develop into mesophases with defined textures, mainly upon cooling from their isotropic melts (Fig. 1), before samples solidify generally above 60 °C.

In some preparations, *schlieren*-type defects were observed (Fig. 1), which are consistent with layered bent-core mesophases, while others showed textures that closely resemble the spherulitic-like domains reported for morphological variations of the helical nanofilament phase (HNF-type) (Fig. 1), with no

detectable texture changes upon cooling at different rates (5° and 20 °C min^{-1}).[56,62,63]

POM observations were in good agreement with phase transition changes in DSC. Unfortunately, some micrographs, even though they showed birefringence and liquid crystalline behaviour, were not useful for phase identification.

Interestingly, the **LiTf$_2$N-TEG-10-B1-14** and **LiTfO-TEG-10-B1-14** complexes display a sequence of two mesophases, supported by both calorimetric and microscopic studies. Although a clear mesophase–mesophase transition could be detected by DSC around 75 °C when cooling **LiTf$_2$N-TEG-10-B1-14** with an enthalpy of $\Delta H \sim 1.4$ kJ mol^{-1}, the appearance of a broad DSC peak in **LiTfO-TEG-10-B1-14** suggests the coexistence of two liquid crystalline organizations detected also by POM, which is
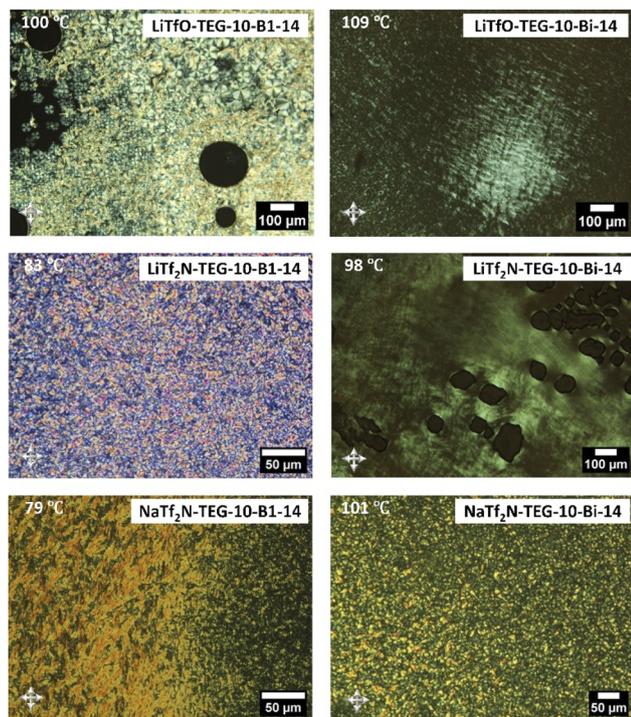
11298 | *J. Mater. Chem. A*, 2026, **14**, 11294–11309

This journal is © The Royal Society of Chemistry 2026

Fig. 1 POM mesophase textures of the complexes observed on cooling; left for **MA-TEG-10-B1-14** series and right for **MA-TEG-10-Bi-14** series. Images of LiTfO- and LiTf$_2$N-Bi-based materials were recorded after mechanical shearing.

not unusual for bent-core compounds.[64–67] However, our results also suggest that complexation with Na$^+$ strongly hinders the formation of liquid crystalline phases, with NaTfO promoting phase separation when mixed with the TEG-based bent-cores. According to our POM observations, only the two **NaTf$_2$N-TEG-10-Bx-14** complexes show monotropic mesophases in a narrow temperature range.

3.2.2 X-ray diffraction studies. X-ray diffraction (XRD) experiments at different temperatures confirmed the non-liquid crystalline nature of **TEG-10-Bx-14** compounds (Fig. S12); alternatively, some of the **MA-TEG-10-Bx-14** complexes show enantiotropic or monotropic liquid crystal behaviour with different mesogenic structures, pointing to different experimental lamellar periodicities c (Table 3).

On cooling from the isotropic liquid to the solid phase, the Li-complexes based on **TEG-10-Bi-14**, i.e. **LiTfO-TEG-10-Bi-14** and **LiTf$_2$N-TEG-10-Bi-14**, the diffraction patterns show a set of harmonic peaks in the small-angle region, assigned to a lamellar arrangement with spacing of 112 and 109 Å, respectively (Table 3). A smectic bilayer structure, i.e., organisations where sets of two layers are periodically distributed, is proposed for both complexes, in agreement with the molecular bent-core unit length (estimated length, 74 Å).

In order to illustrate this, Fig. 2 shows the diffraction pattern of the **LiTfO-TEG-10-Bi-14** complex together with the electronic density map obtained from the diffracted intensities (see SI for calculation details), together with a scheme of the proposed

molecular disposition. When proposing these structural models, it must be considered that the diffraction diagrams are limited to the (00l) line for a lamellar phase; therefore, conventional (non-resonant) XRD does not detect the polarization of layers and sublayers.

Additionally, in the wide-angle region superimposed to the diffuse halo due to the alkyl-chain disorder, the contribution of some reflections could also be identified in both materials (see Fig. 2 and S13 for **LiTfO-TEG-10-Bi-14** and for **LiTf$_2$N-TEG-10-Bi-14**). In agreement with previous well-stated proposals by Hegmann et al.,[63] this type of diagram can be associated with the formation of HNF-like phases, in which the molecules are distributed within the layers with a hexatic in-plane order[47,48,63] although the certainty of the morphological variant is still open for our materials. To gain some insights into the molecular organizations of these Bi-based hybrid materials, transmission electron microscopy (TEM) studies were carried out at their quenched mesophase (Fig. S11), showing that both **LiTfO-TEG-10-Bi-14** and **LiTf$_2$N-TEG-10-Bi-14** materials present structures consistent with HNF-like organizations.[63]

Interestingly, these results once again support the trend of the lateral Bi-moieties to drive helical organisations and interestingly reveal that even an asymmetric bent-core structure with a short lateral unit does not prevent[33,62,68] the layer twisting that generates the characteristic helical nanofilaments of some of these phases.[56,62,63,69,70]

If we now turn our attention to the complexes based on **TEG-10-B1-14**, simpler patterns were observed for **LiTfO-TEG-10-B1-14** and **LiTf$_2$N-TEG-10-B1-14**, with at least three intense harmonic peaks in the small-angle regions and typical diffuse halos in the wide-angle region. Accordingly, polar smectic C liquid crystalline (SmCP) organisations, typical of bent-core molecular packings,[44] have been proposed. Fig. 3 illustrates the diffraction pattern of both materials together with the corresponding electronic density maps and a scheme of the molecular organizations. In this case, we propose smectic monolayer and bilayer structures for **LiTfO-TEG-10-B1-14** and **LiTf$_2$N-TEG-10-B1-14**, respectively, despite having the same bent-core ligand (estimated length, 77 Å), which should be related to the presence of different anions. Furthermore, although XRD could confirm only the stabilization of an SmCP mesophase in these materials, POM and DSC observations suggest the formation of a second liquid crystal organisation in a short range of temperatures on cooling **LiTf$_2$N-TEG-10-B1-14**.

Concerning sodium salts, the largest anion (Tf$_2$N$^-$) seems to stabilise nanostructured soft self-assemblies more efficiently, leading to an undulated smectic phase (USmCP) in the case of the **NaTf$_2$N-TEG-10-B1-14** complex and to an oblique columnar structure (Col$_{ob}$) for the **NaTf$_2$N-TEG-10-Bi-14** complex (Fig. 4). Since the diffraction diagram is now limited to the (h0l) reciprocal plane, conventional (non-resonant) XRD does not detect polarisation along the b axis.

These nanostructures were further assessed by additional room temperature TEM studies carried out on samples quenched from the mesophase on the grid (Fig. S11), revealing the formation of both twisted nanofibers (for Bi-based materials) and nanocylinders (for B1-based materials) morphologies.

This journal is © The Royal Society of Chemistry 2026

J. Mater. Chem. A, 2026, **14**, 11294–11309 | **11299**

Table 3 Scattering vectors of the **MA-TEG-10-Bx-14** complexes showing liquid crystal behaviour measured during cooling processes

Compound	Mesophase (T °C)	d (Å)	Miller index (hkl)	Lattice parameters (Å)
LiTfO-TEG-10-B1-14	SmCP (85)	84.1	001	$c = 86.4$ Å
		42.3	002	
		28.1	003	
		20.8	004	
		17.4	005	
		15.2	006	
		13.2	007	
LiTfO-TEG-10-Bi-14	HNF-like (115)	111	001	$c = 112$ Å
		55.3	002	
		38.0	003	
		28.5	004	
		22.3	005	
LiTf$_2$N-TEG-10-B1-14	SmCP (80)	103.7	001	$c = 104$ Å
		52.2	002	
		34.7	003	
LiTf$_2$N-TEG-10-Bi-14	HNF-like (80)	53.9	200	$c = 109$ Å
		36.9	300	
		31.9	400	
		22.4	005	
NaTf$_2$N-TEG-10-B1-14	USmCP (80)	72.7	001	$a = 54.3$ Å
		43.5	101	$c = 72$ Å
		36.2	002	
		30.3	102	
		17.9	004	
NaTf$_2$N-TEG-10-Bi-14	Col$_{Ob}$ (70)	69.9	100	$a = 92.2$ Å
		33.1	$\bar{1}01$	$c = 35.1$ Å
		20.8	101	$\beta = 130.7°$
		13.3	002	
		8.9	003	

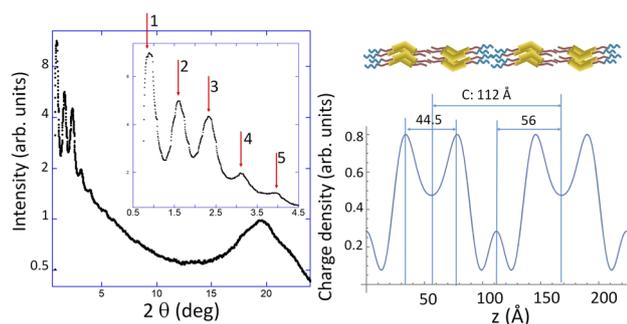**Fig. 2** X-ray diffractogram of the **LiTfO-TEG-10-Bi-14** complex, obtained at 115 °C. The inset represents the small-angle region (reflections indicated 1–5 are (001)–(005)). The diffuse halo in the wide-angle region is not typical of a mesophase, showing the contribution of some reflections. Corresponding charge density map is represented on the right side. Distances revealing the bilayer character of the structure are indicated. z is the coordinate along the smectic layer normal. Yellow, blue, and red regions in the schematic represent the aromatic BC structure, TEG chains and the alkyl tails, respectively.

These results are consistent with previously documented morphologies and transitions observed in bent-core liquid crystalline systems stabilising HNF-like motives, appearing even below the SmC phases.[71–73]

3.2.3 Comparative analysis. Interestingly, the archetypal bent-core design of these new **TEG-10-Bx-14** compounds does not promote liquid crystal order in a similar way to their parent BC-molecules with a direct bent-core/TEG connexion (**TEG-0-Bx-14**).[33,34] Even though the two series show similar melting temperatures, the smaller melting enthalpy changes displayed for the current **TEG-10-Bx-14** compounds (ΔH: 53–56 kJ mol^{-1}) seem to indicate that the introduction of the flexible C10-alkyl spacer promotes more compact packing, somehow decoupling the bent-core structure from the flexible TEG-tail, with respect to the **TEG-0-Bx-14** analogues (ΔH: 60–70 kJ mol^{-1}).[33] However, the formation of liquid crystalline lamellar structures by the **MA-TEG-10-Bx-14** complexes can be attributed to a weakening of the molecular interactions by the presence of the salts, which ultimately facilitates their fluid character.

Remarkably, despite the strong bent-core driving force towards lamellar self-assemblies, a subtle balance between the cation/TEG interactions and the cation/anion dissociation seems to occur in this series of materials. Thus, on ion-complexation, the presence of a long spacer connecting the TEG-segment results in various molecular dispositions. This can result in the intercalation of terminal and inner alkyl tails (similar in chemical nature and with comparable lengths), leading to different TEG-segregation patterns and structural organisations, where significant contributions from bent-core tilting cannot be ruled out. For some complexes, fractions of
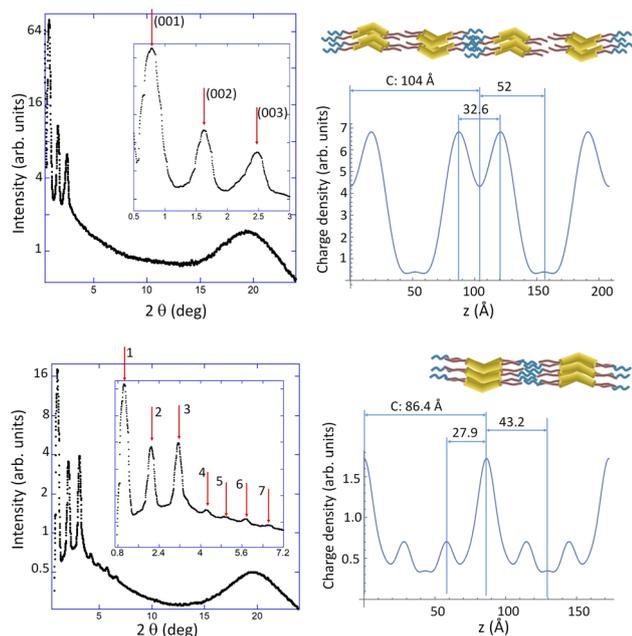
11300 | J. Mater. Chem. A, 2026, **14**, 11294–11309

This journal is © The Royal Society of Chemistry 2026

Fig. 3 X-ray diffractograms of the **LiTf$_2$N-TEG-10-B1-14** (top) and **LiTfO-TEG-10-B1-14** (bottom) complexes at 85 °C; insets represent the small angle regions (reflections indicated 1–7 in the diagram of **LiTfO-TEG-10-B1-14** are (001)–(007)). The wide-angle region shows a typical diffuse halo. Corresponding charge density map is represented on the right side. z is the coordinate along the smectic layer normal. Distances revealing the monolayer or bilayer character of the structures are indicated. Yellow, blue and red regions in the schematic represent the aromatic BC structure, TEG chains and alkyl tails, respectively.
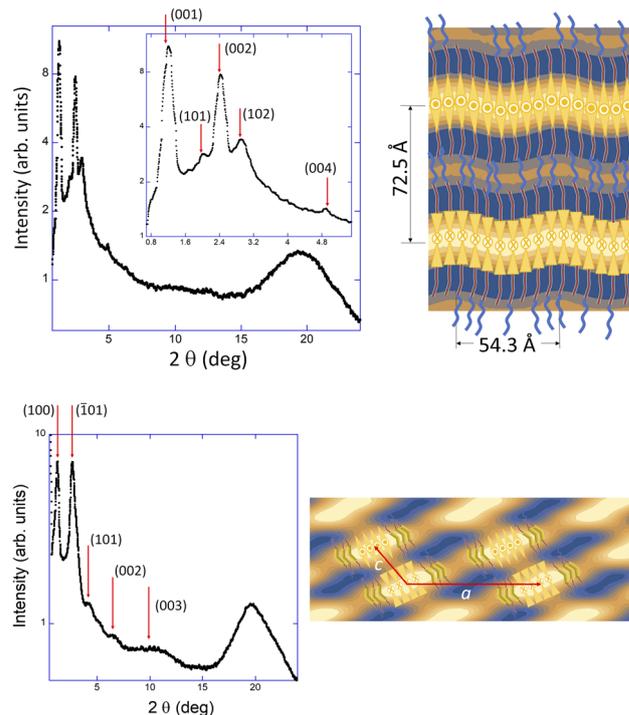
Fig. 4 X-ray diffractograms of the **NaTf$_2$N-TEG-10-B1-14** at 80 °C (top) and **NaTf$_2$N-TEG-10-Bi-14** at 70 °C (bottom) complexes. Inset in the diagram of **NaTf2N-TEG-10-B1-14** represents the small angle region. The corresponding 2D charge density maps show an undulated smectic structure for **NaTf$_2$N-TEG-10-B1-14** and an oblique columnar one with cell parameters of $a = 92.2$ Å, $c = 35.1$ Å and $\beta = 130.7°$ for **NaTf$_2$N-TEG-10-Bi-14**. Yellow, blue and red regions in the molecular schematic represent the aromatic BC structure, TEG chains and alkyl tails, respectively.

the molecules can form segregated sublayers formed by single bent-core mesogens with values close to the estimated molecular lengths. This suggests a strong molecular intercalation in the mesophase, where flexible EO chains are surrounded by alkyl-blocks either from the spacer or terminal tails. However, in other materials, driven by strong core-to-core interactions, well-defined TEG-segment segregation and highly significant intercalation of the terminal alkyl chains occur, thereby stabilising bilayer organizations.[47,48]

According to their mesophase ranges, lithium-based complexes are the most suitable materials for providing liquid crystal organisations within the materials under study. Interestingly, both LiTfO and LiTf$_2$N salts promote short-range HNF-like arrangements upon cooling and bilayer organisation. However, distinctive effects can be pointed out concerning complexes based on the B1/Li-tandem. Along with the enantiotropic character of their liquid crystalline assembly for these materials, mesophase polymorphism is also suitable based on the appearance of SmCP and HNF-like organisations. In complexes containing the smaller TfO$^-$ anion, such phases coexist over a narrow temperature range, whereas a clear first-order transition between the two mesophases can be detected by POM and DSC when a larger Tf$_2$N$^-$ anion is present. Furthermore, a monolayer spacing of $c = 86.4$ Å is determined

for **LiTfO-TEG-10-B1-14** *versus* a bilayer arrangement of $c = 104$ Å for **LiTf$_2$N-TEG-10-B1-14** (Fig. 3).

3.3. Dielectric and conductivity properties

The dielectric loss factor (ε''), relative to the vacuum value (ε_0) measured at different frequencies and temperatures, is evaluated for **TEG-10-B1-14** and **TEG-10-Bi-14** (Fig. S14A and F). The so-called Bode plots of both pristine **TEG-10-Bx-14** materials show one main process with maxima (ε''_{max}) in the mid-frequency regions ($<10^3$ Hz), followed by a secondary process at higher frequencies ($>10^3$ Hz). We can assign the main process to local soft modes of vibration of the compounds in their isotropic phases, which are unaffected by the presence of direct current (DC) electrical fields. This is consistent with our previous findings on bent-core compounds without alkyl spacer, **TEG-0-Bx-14**.[32] Unfortunately, it was not possible to determine the maxima of the ε'' peak through the whole temperature range and the activation energy of the dielectric relaxation could not be estimated. The secondary ε'' peak observed at higher frequencies must be associated with more localised charge transfer effects, such as molecular dipoles, which occur faster.

The rise of ε'' values in the low-frequency range denotes the occurrence of conductivity, when charges are given enough time

This journal is © The Royal Society of Chemistry 2026

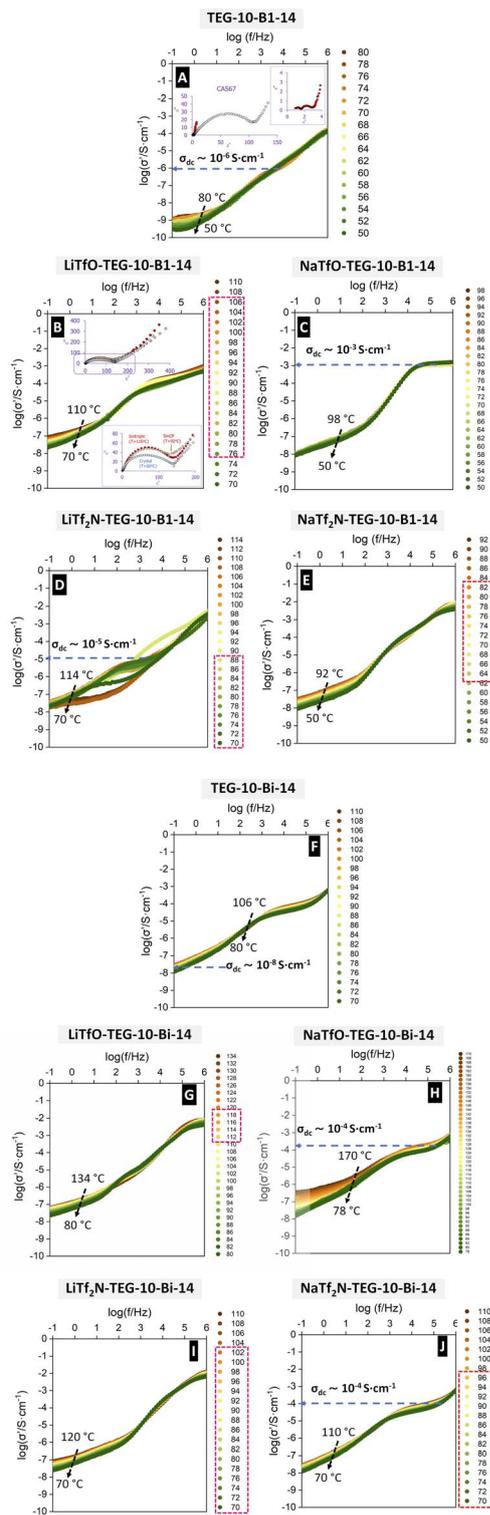*J. Mater. Chem. A*, 2026, **14**, 11294–11309 | **11301**

Fig. 5 Bode plots showing the frequency and temperature dependence of the real component of the complex conductivity (σ') measured for the non-doped and doped samples of the **TEG-10-B1-14** (A–E) and of **TEG-10-Bi-14** (F–J) compounds upon cooling from the corresponding isotropic melts. The range of mesophase is indicated in the red square of temperature legends. Insets in panels A and B show the corresponding Cole–Cole plots (ε'' vs. ε') obtained from the dielectric/conductivity measurements.

to transfer between electrodes. Plots of the real component of the complex conductivity (σ'), obtained using eqn (3) (Subsection 2.4.) for the pristine compounds **TEG-10-Bx-14**, are shown in Fig. 5A and F. It is possible to observe plateau regions in the double logarithmic plots at both low and medium frequencies, which are representative of direct current (DC) conductivity (σ_{dc}). The σ_{dc} can be estimated by extrapolating these plateaus to log(f/Hz $\to$ 0). We can acknowledge that DC conductivity is already happening in these samples, even though some plateaus are ill-defined.

The nature of the conductivity in the samples was preliminarily assessed through their Cole–Cole plots (ε'' vs. ε'), which can provide comparable information as impedance Nyquist plots (Z'' vs. Z') in samples with a marked dielectric response. Selected examples are shown as insets in Fig. 5 and SI15. Most of the samples display a semicircle (at high frequencies), followed by a linear region (at low frequencies), typical of the re-orientation of dipoles in solid electrolytes.[74,75] The single broad depressed semicircle can be associated with bulk (and/or interfacial) relaxations. Its distortion (from an ideal semicircle) can be due to heterogeneities in the bent-core systems. The appearance of a second semicircle in some cases may denote interfacial and grain-boundary processes. The low-frequency rise, however, is related to ionic diffusion. These results confirm that conductivity through the **TEG-BX-10-14** bent-core materials and complexes is a combination of multiple charges (see the dielectric relaxations in Fig. S14) and ionic diffusion phenomena. It is also worth noting that temperature influences the shape of the Cole–Cole plots, which is consistent with the variations in the dielectric and conductivity curves. **LiTFS-TEG-10-B1-14**, for example, shows slightly different shapes in its three phases (isotropic, SmCP and crystal), see Fig. 5B. Although such differences are rather subtle and their study goes beyond the scope of the present paper, our observations can trigger more exhaustive research on the correlation between phase structure and conductivity mechanisms in liquid crystalline materials.

Based on the dielectric and conductivity data reported herein, four main effects are addressed.

3.3.1 Effect of salt addition. As expected, the addition of the alkali salts promotes changes in the dielectric response of the TEG-based materials owing to the presence of new polar sites and alterations within the microstructure. In general, the ε'' and σ' signals increase, which can be explained by the introduction of new charges carried by the ions. First, the increase in the ε'' values in the low-frequency region is generalised in all complexes (from ε'' of 10/100 to around 1000), denoting an enhancement of long-range DC conductivity (<10[1] Hz), which is visible in σ' jumps from σ_{dc} ~10^{-9}/10^{-8} S cm^{-1} to the 10^{-7} S cm^{-1} range. We note that these values are in the range of other liquid crystalline electrolytes,[18] reaching σ_{dc} ~10^{-4} S cm^{-1} in the mid-high frequency range, but still have low values, particularly compared to electrolytes used in commercial devices (~10^{-1} S cm^{-1}). Furthermore, the introduction of the salts results in multiple dielectric and conductivity processes at mid and high frequencies, which are visible in the Cole–Cole plots. Even though it is difficult to generalise

11302 | J. Mater. Chem. A, 2026, **14**, 11294–11309

This journal is © The Royal Society of Chemistry 2026

for all samples under study, we observe an increase of ε'' in the high frequency range, with multiple maxima located around the $10^3/10^6$ Hz region. In some cases, ill-defined plateaus in the σ' curves are also visible, which denote short-range DC conductivity processes and may be attributed to the motion of the ions within the microstructure of the salts.

3.3.2 Effect of promesogenic structure. There is no evident correlation between the chemical structure of the TEG-bent-core moiety and the conductivity of the corresponding alkali complexes. It is worth mentioning, however, that in the low-frequency end, the ester-based **TEG-B1-10-14** shows lower conductivity values with respect to the biphenyl-based analogous, **TEG-Bi-10-14**. When adding the MA salts, however, complexes containing both bent-core molecules show comparable results in the mid- and high-frequency ranges despite the type of lamellar mesophase.

3.3.3 Effect of cation. Although Na-ion containing samples exhibit prominent high-frequency dielectric and conductivity processes, samples doped with Li-ions seem to promote mid-frequency conductivity response. These processes can also be attributed to the formation of liquid crystalline phases, which occur in all our lithium-containing compounds complexed with TfO⁻. These results are also consistent with those obtained previously when the **TEG-0-Bx-14** analogues (without the C10 alkyl spacer) are complexed with LiTfO.

3.3.4 Effect of anion. There is no clear correlation between the type of counter-anion used and the conductivity and dielectric response of the **MA-TEG-10-Bx-14** complexes. This result is somehow surprising since the reported conductivity values for other ionic liquids and salts depend strongly on the size and nucleophilicity of the anion used.[40,76–78] Normally, we expect that smaller anions (in this case TfO⁻) may allow for higher molecular and ionic mobility. Although this must be true for isotropic melts, it is clear that morphology and nano-structure factors may play an important role in defining conductivity in crystals and liquid crystal states. Tf₂N⁻, for example, although larger than TfO⁻, seems to support the formation of liquid crystalline phases, which may have positive effects on conductivity.

The conductivity values obtained for these new **MA-TEG-10-Bx-14** complexes are within the same range as those obtained for other ionic liquid crystals containing Tf₂N ions and more specifically for asymmetric viologen bistriflimide salts forming smectic *T* phases.[71] In both systems, the conductivity at low frequencies is very low ($<10^{-7}$ S cm^{-1}), which we attributed, in part, to the lack of alignment of ionic channels within the layered nanostructure required to allow for long-term ionic motion and which we also observed in side-chain liquid crystals forming block copolymers.[79]

Intriguingly, we measured the conductivity of our Li-based complexes again after one year to assess potential room-temperature annealing effects and we found that the low-frequency response was enhanced for most of our samples. The σ' plots displayed clear plateaus with considerable temperature dependence, as shown in Fig. 6. This effect seems to be more prominent in B1-based materials and does not seem to be accompanied by the strong homeotropic alignment effects
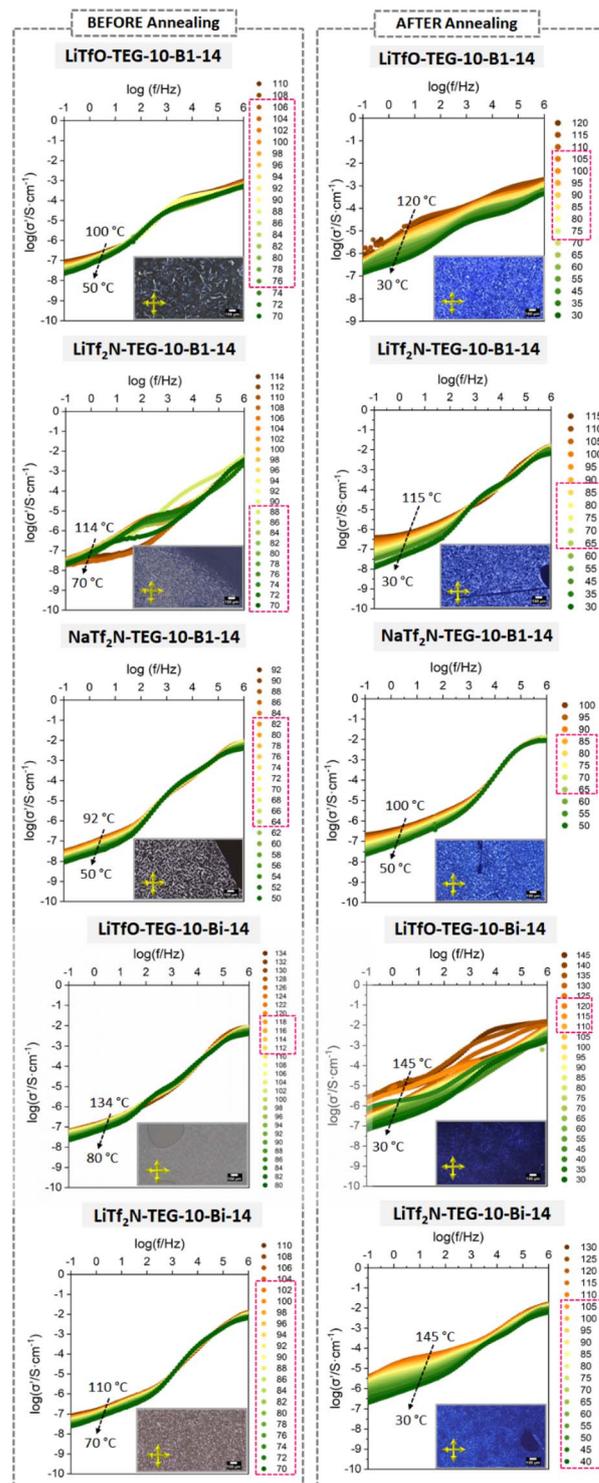

Fig. 6 Bode plots showing the frequency and temperature dependence of the real component of the complex conductivity (σ') of some MA-TEG-10-B1-14 and MA-TEG-10-Bi-14 complexes measured before (left) and after (right) 12 months of annealing at room temperature upon cooling from the corresponding isotropic melts, and their POM mesophase textures. The range of mesophase is indicated in the red square of temperature legends.

visible in POM. Even though a much more detailed annealing study should be carried out, these results could reflect certain rearrangements of the lamellae formed by the bent-core units, facilitated with time, which can open new strategies to ultimately improve the long-range conductivity in ionic samples using the fluidity and anisotropy of liquid crystal phases.

3.4. NMR characterisation of the LiTfO-TEG-10-B1-14 complex

Solid state NMR spectroscopy is used to determine three-dimensional structures of these types of materials and their dynamics. The analysis of the perturbations of the NMR chemical shift of the spectra can be used in the solid state to characterise binding sites and intermolecular interactions. Hence, explorative isothermal PFG experiments are carried out for the **LiTfO-TEG-10-B1-14** complex by heating the sample to its melt liquid state, 120 °C and then cooling to room temperature, measuring at $T = 120°$, $100°$, $85°$, $60°$ and 30 °C. These temperatures are chosen based on the phase transitions observed by DSC. The sample goes from isotropic liquid to mesophase around 91°–92 °C and remains in mesophase until 73°–74 °C when it solidifies. Once the sample solidified, a second cooling cycle was carried out from the sample's isotropic melt. The results are presented in Table 4. By fitting the attenuation curve with the gradient, the diffusion coefficient D_{PFG} of lithium (speed of motion of lithium atoms diffusing between sites in the phase network) was obtained. The initial point at 27 °C has a value of 2.46×10^{-12} m^2 s^{-1} that is not recovered within the first cooling cycle. In both cycles, the coefficient decreases when cooling down the sample.

At intermediate temperatures (60–100 °C range), the D_{PFG} values are very similar. At 27–30 °C, a slightly higher diffusion coefficient (3.85×10^{-13} vs. 2.31×10^{-13} m^2 s^{-1}) is obtained in the first cooling treatment. The diffusion coefficient at 120 °C presents the highest value (1.05×10^{-11} m^2 s^{-1}) during the first cooling cycle, which is almost an order of magnitude higher than that obtained at 393 K in the second cooling cycle (4.22×10^{-12} m^2 s^{-1}). Our results fall within those exhibited by other multi-ionic lithium salts.[80]

Additionally, using the Arrhenius equation, we determined the activation energy, E_a, of the process:

$$D = D_0 \exp\left(\frac{E_a}{KT}\right) \qquad (5)$$

where D_0 is a pre-exponential factor, T is the temperature in kelvin and K is the Boltzmann constant. In the first cooling cycle, an $E_a = 0.359$ eV (35 kJ mol^{-1}) value is obtained, which slightly decreases in the second cycle to $E_a = 0.345$ eV (33 kJ mol^{-1}). These values are lower than those obtained for the ionic conductivity of the lithium-ion, indicating that ionic conductivity can be favoured by temperature increase without incurring much energy expense. Our results indicate that the diffusion coefficient values are good compared to other materials,[80] with diffusion mechanisms that are favoured by the liquid crystal phase transition.

3.5. Gel self-assembled materials

Physical gels represent a very attractive alternative to "bulk" liquid crystalline phases to form self-structured soft electrolytes. Gels are booming for technological applications since they are easy to prepare, thermally reversible and responsive to very varied stimuli, which allows for easy modulation of their properties,[81–84] particularly in flexible energy storage systems (FESS).[6]

Attempts to transfer the characteristic molecular order of bent-core mesophases and therefore their properties to gels have been reported in the last decade.[33,85,86] Continuing with our prospective studies of bent-core gelators, we now explore the self-assembly abilities in organic liquids of the new amphiphilic **TEG-10-Bx-14** compounds and their salt-doped complexes **MA-TEG-10-Bx-14**. Although **TEG-10-Bx-14**-based compounds formed stable gels in the organic solvents under study, 1-octanol and n-dodecane, the **MA-TEG-10-Bx-14** complexes were able to gel 1-octanol only. Furthermore, prospective concentration studies performed in 1-octanol and n-dodecane demonstrate that stable gels are formed from 0.2 wt.% to 3 wt.%, revealing their supergelator character, where the molecules of solvent may establish strong interactions with the hydrocarbon chains of the bent-core amphiphiles.

In order to check the nanostructure and morphology of the three-dimensional networks of these organogels, TEM and XRD experiments were performed. These techniques show that the new amphiphiles, **TEG-10-Bx-14** compounds, form long fibrillar self-assemblies by the in-layer packing of the bent-core building blocks (Fig. 7), which is in good agreement with our previous studies.[33]

In n-dodecane, gels of both **TEG-10-Bx-14** compounds show long tubular fibres (Fig. 7) with outer diameters in the range of

Table 4 Diffusion coefficients (DPFG) of **LiTfO-TEG-10-B1-14** at different temperatures for two cooling cycles

T (°C)	$1000/T$ (K^{-1})	1st cooling cycle		2nd cooling cycle	
		D_{PFG} (m^2 s^{-1})	Ln D_{PFG} (m^2 s^{-1})	D_{PFG} (m^2 s^{-1})	Ln D_{PFG} (m^2 s^{-1})
120	2.54452926	1.05×10^{-11}	-25.28250	4.22×10^{-12}	-26.19118
110	—	—	—	4.14×10^{-12}	-26.21032
100	2.68096515	3.37×10^{-12}	-26.41699	3.14×10^{-12}	-26.48679
85	2.79329609	1.73×10^{-12}	-27.08232	1.95×10^{-12}	-26.96319
60	3.003003	8.45×10^{-13}	-27.79943	8.52×10^{-13}	-27.79119
30	3.33333333	3.85×10^{-13}	-26.73126	2.31×10^{-13}	-29.09636

11304 | J. Mater. Chem. A, 2026, **14**, 11294–11309

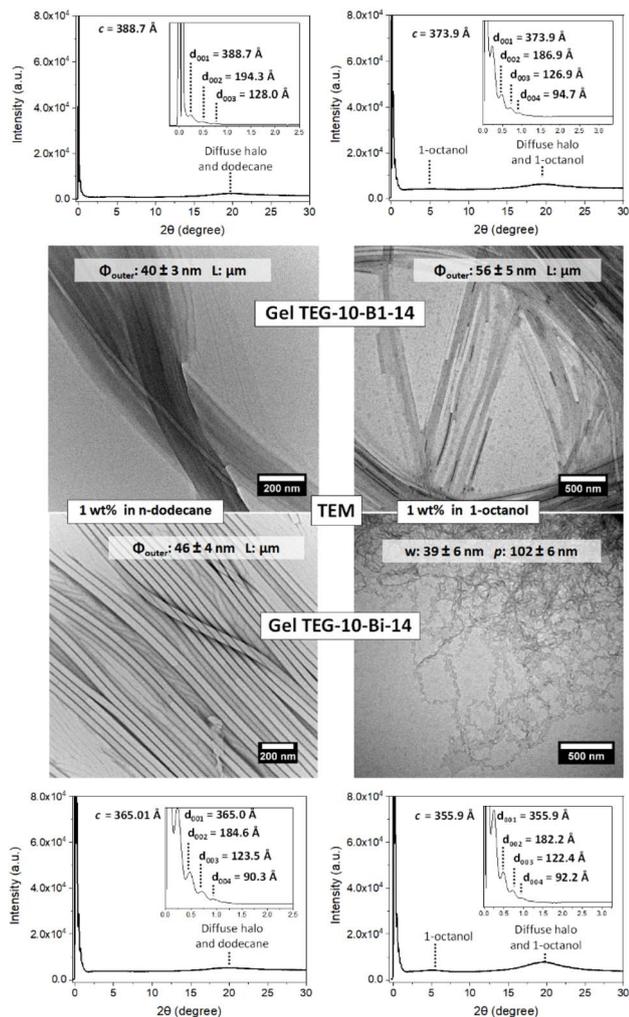This journal is © The Royal Society of Chemistry 2026

Fig. 7 Gels of the **TEG-10-B1-14** (up) and **TEG-10-Bi-14** (down) compounds at 1 wt.% in *n*-dodecane (left) and 1-octanol (right): TEM images showing morphology and fibre parameters [diameter (Φ_{outer}), length (*L*) of the tubules; width (*w*) and pitch (*p*) of the left- and right-handed helical nanoribbons]. XRD diffractogram and patterns from fibres at room temperature. At the small-angle region, enlarged in the inset, a series of periodic peaks appear, which correspond to a layer structure of the gel. Additional broad reflections with the dimensions of the solvent molecule are observed in the middle and wide angles.
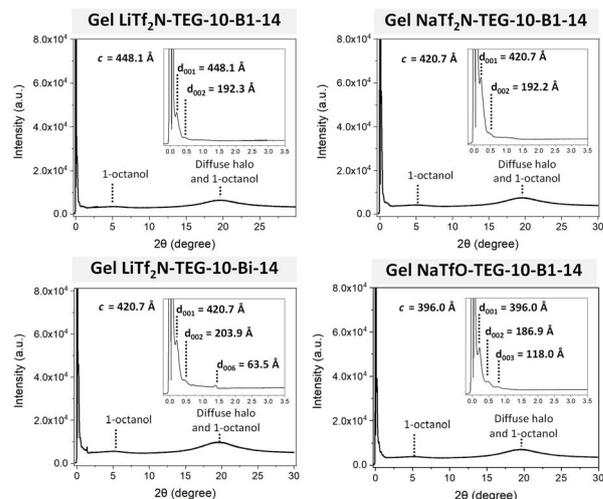

Fig. 8 XRD diffractogram and patterns from the fibres of representative gels based on complexes **MA-TEG-10-Bx-14** at 1 wt% in 1-octanol at room temperature. At the small-angle region enlarged in the inset, a series of periodic peaks appear, which correspond to the layer structure of the gel. Additional broad reflections with the dimensions of the solvent molecule are observed in the middle and wide angles.

that the complexation of alkali atoms helps maintain the layered structures but to a lesser extent than in non-doped gels. Nevertheless, neither dimensions nor differences can be justified because of the molecular length of the **TEG-10-Bx-14** gelators (approximately 77 Å (B1) and 74 Å (Bi)). Additionally, the XRD reflections of all these gels superimposed an intense broad peak at around 19° and a diffuse peak at around 6° for gels based on 1-octanol, which are related to the length of the solvent molecules. As previously proposed for parent TEG-decorated gelators,[33] a significant intercalation of solvent molecules within the layered structure is necessary to explain the large layer spacing. Even though several models for smectic layer self-assembly can explain the current experimental results concerning the formation of fibres, considering the width *w* and diameter Φ dimensions estimated from TEM observations (Fig. S16), we propose that, in these materials, both hollow tubes and helical fibres are built by two bent-core molecules coupled by the TEG-tails, with the alkyloxy tails facing the hydrocarbon-based solvents. Thus, the inside and outside of the tubules or helical ribbons consist of aliphatic chains and solvent molecules, as proposed for parent **TEG-0-Bx-14** gelators.[33]

We preliminarily explored the potential of 1-octanol-based electrolyte gels as alternative soft-conductive materials.[6,87,88] Fig. 9 shows Bode plots for the real conductivity, σ', obtained for gels of **LiTfO-TEG-10-Bi-14** and **LiTfO-TEG-10-B1-14** as representative examples (see also Fig. S17 for the corresponding dielectric loss factor ε'' plots). Notably, their response is comparable to that obtained for the complexes in the absence of solvent (Section 3.3), with even higher DC conductivity values, $\sigma_{dc} \sim 10^{-3}$ S cm^{-1} than the original bulk materials. These results point out that structured gels with

40 nm, while 1-octanol-based gels lead to some differences depending on the bent-core amphiphile. Thus, molecules containing the B1-fragment promote the formation of tubular structures, while the Bi-structure fosters the formation of right- and left-handed helical fibres, with no remarkable differences between the gels formed without or with cation-doping.

Despite their fibrillar morphology, both the **TEG-10-Bx-14**-based gels and those from the **MA-TEG-10-Bx-14** complexes show similar lamellar organisations with (00*l*) periodic peaks in the small-angle region (Fig. 7 and 8). Although layer spacing from 360–380 Å was estimated for **TEG-10-Bx-14**-based gels, larger lamellar packing was observed in their analogous complexes falling within the 400–450 Å range. We hypothesise

This journal is © The Royal Society of Chemistry 2026

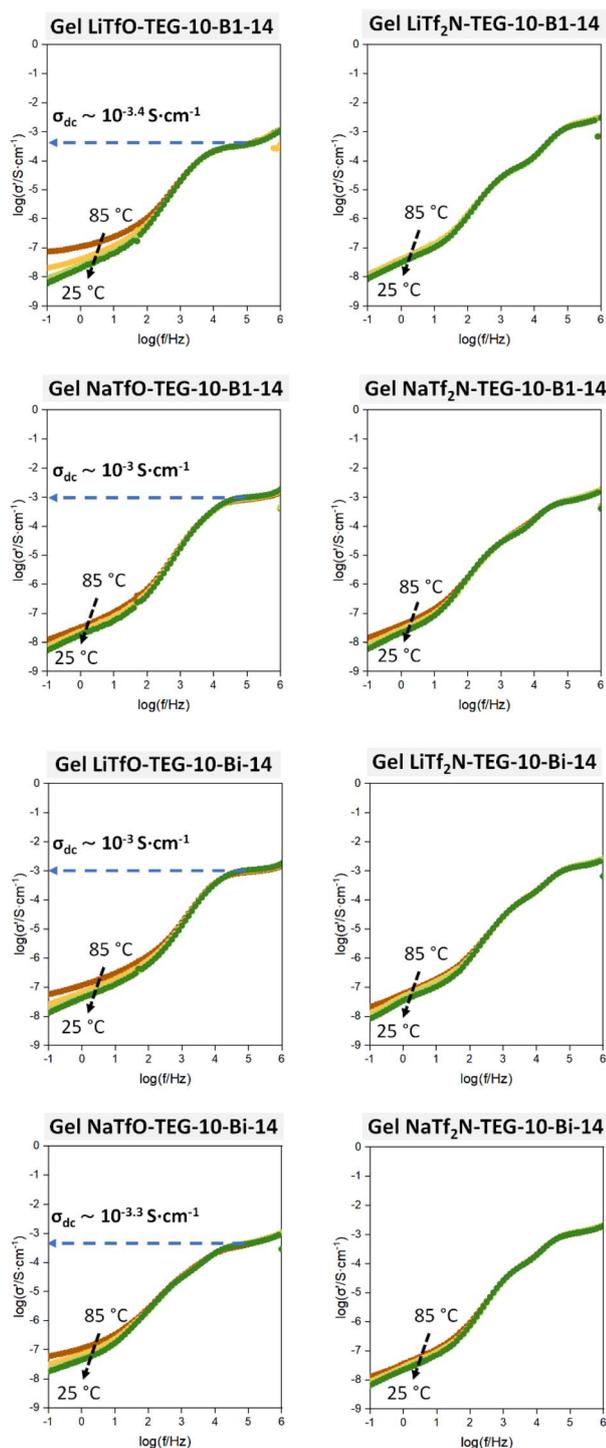*J. Mater. Chem. A*, 2026, **14**, 11294–11309 | **11305**

Fig. 9 Bode plots showing the frequency and temperature dependence of the real component of the complex conductivity (σ'), measured for 1 wt% of the **MA-TEG-10-B1-14** complexes and **MA-TEG-10-Bi-14** gels in 1-octanol upon cooling from the corresponding isotropic solutions to gel at room temperature.

promising ion mobility can be prepared using bent-core amphiphiles with Li and Na-ions and this will be further explored in dedicated follow-up work.

4 Conclusions

We successfully developed a wide range of new structured soft-electrolytes based on two new tetraethylene (TEG)-containing bent-core molecules, which acted as suitable versatile supra-molecular building blocks, their complexes with lithium and sodium salts and their organogels in 1-octanol and *n*-dodecanol. Although the pristine bent-core materials, **TEG-10-Bx-14**, did not show mesomorphism, a combination of various experimental techniques has confirmed selective complexation of the cations in the TEG-region, which further supports self-assembly and the formation of liquid crystalline phases in some of the **MA-TEG-10-Bx-14** complexes. More specifically, an attractive number of bent-core liquid crystalline phases (SmCP, HNF-like, USmCP and Col$_{ob}$) are established, particularly in Li-based complexes. Despite the strong bent-core driving force towards lamellar self-assemblies, a subtle balance between the salt/TEG interactions as well as the cation/anion dissociation seems to occur, weakening the molecular interfaces and promoting fluid order.

On ion-complexation, the presence of a long spacer connecting the TEG-segment with the bent-core of the molecules distinctively results in various molecular dispositions in the liquid crystal phase. For some complexes, fractions of the molecules can form segregated sublayers formed by single bent-core mesogens, where flexible EO chains are surrounded by alkyl-blocks either from the spacer or terminal tails. In other materials, however, well-defined TEG-segment segregations and highly significant intercalation of the terminal alkyl chains and bilayer organisations are stabilised probably driven by strong core-to-core interactions.

All the new bent-core-based materials show a strong dielectric response due to the presence of polarisable groups, which is enhanced after complexation with the ionic pairs. The samples display moderate conductivities comparable to those of other liquid crystals,[6,85,86] which reach $\sim 10^{-4}$ S cm^{-1} in the mid-high frequency range, without an obvious correlation between the salt used for complexation and the conductivity response. Further assessment of the lithium diffusion coefficient, D_{PFG}, carried out by solid state NMR spectroscopy has confirmed that ion mobility is favoured through the liquid crystal phase transition.

In addition, all the new materials under study form organogels of non-polar solvents, such as 1-octanol and *n*-dodecane, even at very low concentrations, leading to highly demanded supramolecular nanostructures, from helical fibres to tubules, depending on both the gelator and the solvent. In particular, 1-octanol gels have demonstrated potential as soft-electrolytes, with comparable (or even greater) conductivities than those obtained for the **MA-TEG-10-Bx-14** complexes in the absence of solvents.

Interestingly, some additional experiments carried out have shown that sample annealing at room temperature of complexes for several months can improve the low-frequency response of these materials. This intriguing observation confirms the possibility of using the fluidity of the liquid crystal

11306 | *J. Mater. Chem. A*, 2026, **14**, 11294–11309

This journal is © The Royal Society of Chemistry 2026

phases to optimise the channels responsible for ionic transport in the long-term and their application as smart electrolytes using a combination of organic cations with lithium and sodium. Further correlation between microstructure and conductivity models is the object of future work. Thus, our results open new venues to yield structured soft-electrolytes containing Li and Na-ions, which can provide sustainable solutions for flexible energy conversion and storage devices.

Author contributions

Carlota Auria-Soro: synthesis and structural and functional characterisation of the compounds and hybrid-materials, investigation, methodology and writing. Nuria Cruz-Navarro: synthesis of the compounds and hybrid-materials. César L. Folcia: X-ray characterization of mesophases, investigation, writing and review. Isabel Sobrados: NMR characterisation, writing and review. Amin Sharifi: functional characterization, writing & review. Alfonso Martinez-Felipe: functional characterization, funding acquisition, writing, review and editing. M Blanca Ros: conceptualisation, coordination, funding acquisition, writing, review and editing. All authors have given approval to the final version of the manuscript.

Conflicts of interest

There are no conflicts to declare.

Data availability

Supplementary information (SI): experimental details, synthetic routes, and full characterization data for the bent-core compounds and their alkali metal-containing complexes, including data from solution and solid-state NMR (^{1}H, ^{13}C CP-MAS, ^{1}H MAS and ^{7}Li MAS), FTIR spectroscopy, thermal analysis (DSC and TGA), POM, XRD, TEM, and dielectric spectroscopy measurements. See DOI: https://doi.org/10.1039/d5ta09556e.

Acknowledgements

References

1 L. Hultman, S. Mazur, C. Ankarcrona, A. Palmqvist, M. Abrahamsson, M.-L. Antti, M. Baltzar, L. Bergström, P. de Laval, L. Edman, P. Erhart, L. Kloo, M. W. Lundberg, A. Mikkelsen, E. Moons, C. Persson, H. Rensmo, J. Rosén, C. Rudén, M. Selleby, J.-E. Sundgren, K. Dick Thelander, K. Tybrandt, P. Weihed, X. Zou, M. Åstrand, C. P. Björkman, J. M. Schneider, O. Eriksson and M. Berggren, *Nat. Mater.*, 2024, **23**, 160–161.

2 J. Liang, J. Luo, Q. Sun, X. Yang, R. Li and X. Sun, *Energy Storage Mater.*, 2019, **21**, 308–334.

3 E. Pomerantseva, F. Bonaccorso, X. Feng, Y. Cui and Y. Gogotsi, *Science*, 2019, **366**, 969.

4 J. He, L. Cao, J. Cui, G. Fu, R. Jiang, X. Xu and C. Guan, *Adv. Mater.*, 2024, **36**, 2306090.

5 J. C. Barbosa, R. S. Pinto, J. P. Serra, C. M. Costa, S. Lanceros-Mendez and R. Gonçalves, *J. Mater. Chem. A*, 2025, **13**, 35952–35975.

6 T. Shui, Y. Liang, T. Wejrzanowski, J. Liu, S.-Z. Kure-Chu, T. Hihara, T. Zhang, F. Liang, C. Sun, W. She, W. Zhang and Z. M. Sun, *Chem. Rev.*, 2025, **125**, 7167–7222.

7 O. Borodin, *Curr. Opin. Electrochem.*, 2019, **13**, 86–93.

8 J. Zhang, J. Li, H. Wang and M. Wang, *Front. Chem.*, 2023, **11**, 1253959.

9 D. Zhu, Y. Ren, Y. Yu, L. Zhang, Y. Wan, H. Wang, W. Gao, B. Han and L. Zhang, *ChemElectroChem*, 2023, **10**, e202300009.

10 G. Wang, X. Guo, J. Chen, P. Han, Q. Su, M. Guo, B. Wang and H. Song, *Energy*, 2023, **16**, 6346.

11 B. K. Cho, *RSC Adv.*, 2014, **4**, 395–405.

12 T. Kato, M. Yoshio, T. Ichikawa, B. Soberats, H. Ohno and M. Funahashi, *Nat. Rev. Mater.*, 2017, **2**, 1–20.

13 T. Kato, M. Gupta, D. Yamaguchi, K. P. Gan and M. Nakayama, *Bull. Chem. Soc. Jpn.*, 2021, **94**, 357–376.

14 J. Uchida, B. Soberats, M. Gupta and T. Kato, *Adv. Mater.*, 2022, **34**, 2109063.

15 H. K. Bisoyi and Q. Li, *Chem. Rev.*, 2022, **122**, 4887–4926.

16 I. Álvarez Moisés, A. Innocenti, M. Somville, B. Notredame, S. Passerini and J. F. Gohy, *MRS Adv.*, 2023, **8**, 797–802.

17 X. Wang, R. Yan, H. Niu, Z. He, W. He and Z. Miao, *J. Energy Storage*, 2024, **100**, 113687.

18 S. Liu, L. Zhou, Y. Zheng and K. Neyts, *EES Batter.*, 2025, **1**, 999–1046.

19 K. Goossens, K. Lava, C. W. Bielawski and K. Binnemans, *Chem. Rev.*, 2016, **116**, 4643–4807.

20 K. Salikolimi, A. A. Sudhakar and Y. Ishida, *Langmuir*, 2020, **36**, 11702–11731.

This journal is © The Royal Society of Chemistry 2026

J. Mater. Chem. A, 2026, **14**, 11294–11309 | **11307**

21 N. Kapernaum, A. Lange, M. Ebert, M. A. Grunwald, C. Haege, S. Marino, A. Zens, A. Taubert, F. Giesselmann and S. Laschat, *ChemPlusChem*, 2022, **87**, e202100397.

22 Q. Ruan, M. Yao, D. Yuan, H. Dong, J. Liu, X. Yuan, W. Fang, G. Zhao and H. Zhang, *Nano Energy*, 2023, **106**, 108087.

23 V. Molahalli, P. Hirankittiwong, A. Sharma, H. Laeim, A. Shetty, N. Chattham and G. Hegde, *Mater. Sci. Eng. B*, 2024, **305**, 117369.

24 Ashy and M. Gupta, *J. Mol. Liq.*, 2025, **419**, 126740.

25 Z. Xue, D. He and X. Xie, *J. Mater. Chem. A*, 2015, **3**, 19218–19253.

26 T. S. Dörr, A. Pelz, P. Zhang, T. Kraus, M. Winter and H. D. Wiemhöfer, *Chem. – Eur. J.*, 2018, **24**, 8061–8065.

27 S. Venkatesan, I. P. Liu, J. C. Lin, M. H. Tsai, H. Teng and Y. L. Lee, *J. Mater. Chem. A*, 2018, **6**, 10085–10094.

28 T. N. T. Phan, S. Issa and D. Gigmes, *Polym. Int.*, 2019, **68**, 7–13.

29 S. Tang, W. Guo and Y. Fu, *Adv. Energy Mater.*, 2021, **11**, 2000802.

30 J. C. Wang, X. Y. Liu, N. Zhang, P. F. Wang, Y. R. Zhu, J. Shu, C. S. Li and T. F. Yi, *Mater. Chem. Front.*, 2024, **8**, 3446–3463.

31 A. Pipertzis, G. Zardalidis, K. Wunderlich, M. Klapper, K. Müllen and G. Floudas, *Macromolecules*, 2017, **50**, 1981–1990.

32 Y. Chang, Y. Jiao, H. E. Symons, J. F. Xu, C. F. J. Faul and X. Zhang, *Chem. Soc. Rev.*, 2019, **48**, 989–1003.

33 M. Castillo-Vallés, C. L. Folcia, J. Ortega, J. Etxebarria and M. B. Ros, *J. Mol. Liq.*, 2023, **381**, 121825.

34 A. Martinez-Felipe, D. Zaton, M. Castillo-Vallés, A. Baldini, J. Pease, N. Leader, N. F. Kamalul Aripin, M. Giacinti-Baschetti and M. Blanca Ros, *J. Mol. Liq.*, 2023, **390**, 123100.

35 J. Etxebarria and M. B. Ros, *J. Mater. Chem.*, 2008, **18**, 2919–2926.

36 I. C. Pintre, J. L. Serrano, M. B. Ros, J. Martínez-Perdiguero, I. Alonso, J. Ortega, C. L. Folcia, J. Etxebarria, R. Alicante and B. Villacampa, *J. Mater. Chem.*, 2010, **20**, 2965–2971.

37 H. Takezoe, *Mol. Cryst. Liq. Cryst.*, 2017, **646**, 46–65.

38 K. I. Shivakumar, D. Pociecha, J. Szczytko, S. Kapuściński, H. Monobe and P. Kaszyński, *J. Mater. Chem. C*, 2020, **8**, 1083–1088.

39 M. Martínez-Abadía, S. Varghese, J. Gierschner, R. Giménez and M. B. Ros, *J. Mater. Chem. C*, 2022, **10**, 12012–12021.

40 Z. Huang, X. Li, Z. Chen, P. Li, X. Ji and C. Zhi, *Nat. Rev. Chem.*, 2023, **79**, 616–631.

41 S.-Y. Li, Y.-L. Heng, Z.-Y. Gu, X.-T. Wang, Y. Liu, X.-R. Zhang, Z.-H. Sun, D.-H. Liu, B. Li and X.-L. Wu, *Chem. Sci.*, 2026, **17**, 137–150.

42 Y. Huang, L. Zhao, L. Li, M. Xie, F. Wu and R. Chen, *Adv. Mater.*, 2019, **31**, 1808393.

43 C. Tschierske, *Angew. Chem., Int. Ed.*, 2013, **52**, 8828–8878.

44 R. A. Reddy and C. Tschierske, *J. Mater. Chem.*, 2006, **16**, 907–961.

45 H. Takezoe and Y. Takanishi, *Jpn. J. Appl. Phys. Pt. 1*, 2006, **45**, 597–625.

46 Ń. Gimeno, J. Barbeŕa, J. L. Serrano, M. B. Ros, M. R. De La Fuente, I. Alonso and Ć. L. Folcia, *Chem. Mater.*, 2009, **21**, 4620–4630.

47 I. Dierking, *Liq. Cryst. Today*, 2015, **24**, 93–95.

48 H. Takezoe and A. Eremin, *Bent-Shaped Liquid Crystals : Structures and Physical Properties*, CRC Press, Boca Raton, 2017.

49 M. Nagaraj, *Liq. Cryst.*, 2016, **43**, 2244–2253.

50 C. Tschierske and G. Ungar, *ChemPhysChem*, 2016, **17**, 9–26.

51 K. V. Le, H. Takezoe and F. Araoka, *Adv. Mater.*, 2017, **29**, 1602737.

52 S. Kaur, V. Punjani, N. Yadav, A. Barthakur, A. Baghla, S. Dhara and S. K. Pal, *Liq. Cryst.*, 2022, **49**, 1078–1146.

53 N. Gimeno, M. B. Ros, J. L. Serrano and M. R. de la Fuente, *Angew. Chem.*, 2004, **43**, 5235–5238.

54 D. Kardas, M. Prehm, U. Baumeister, D. Pociecha, R. Amaranatha Reddy, G. H. Mehl and C. Tschierske, *J. Mater. Chem.*, 2005, **15**, 1722–1733.

55 C. L. Folcia, I. Alonso, J. Ortega, J. Etxebarria, I. Pintre and M. B. Ros, *Chem. Mater.*, 2006, **18**, 4617–4626.

56 E. Tsai, J. M. Richardson, E. Korblova, M. Nakata, D. Chen, Y. Shen, R. Shao, N. A. Clark and D. M. Walba, *Angew. Chem., Int. Ed.*, 2013, **52**, 5254–5257.

57 N. Gimeno, I. Pintre, M. Martínez-Abadía, J. L. Serrano and M. B. Ros, *RSC Adv.*, 2014, **4**, 19694–19702.

58 S. P. Gejji, K. Hermansson, J. Tegenfeldt and J. Lindgren, *J. Phys. Chem.*, 1993, **97**, 11402–11407.

59 A. G. Bishop, D. R. MacFarlane, D. McNaughton and M. Forsyth, *Solid State Ionics*, 1996, **85**, 129–135.

60 A. G. Bishop, D. R. MacFarlane, D. McNaughton and M. Forsyth, *J. Phys. Chem.*, 1996, **100**, 2237–2243.

61 J. Stygar, G. Żukowska and W. Wieczorek, *Solid State Ionics*, 2005, **176**, 2645–2652.

62 J. Liu, S. Shadpour, M. E. Prévôt, M. Chirgwin, A. Nemati, E. Hegmann, R. P. Lemieux and T. Hegmann, *ACS Nano*, 2021, **15**, 7249–7270.

63 A. Gowda, G. Acharjee, S. K. Pathak, G. A. R. Rohaley, A. Shah, R. P. Lemieux, M. E. Prévôt and T. Hegmann, *Mater. Horiz.*, 2024, **11**, 5550–5563.

64 C. Keith, A. Lehmann, U. Baumeister, M. Prehm and C. Tschierske, *Soft Matter*, 2010, **6**, 1704–1721.

65 Y. Zhang, U. Baumeister, C. Tschierske, M. J. O'Callaghan and C. Walker, *Chem. Mater.*, 2010, **22**, 2869–2884.

66 M. Alaasar, M. Prehm, M. Poppe, M. Nagaraj, J. K. Vij and C. Tschierske, *Soft Matter*, 2014, **10**, 5003–5016.

67 M. Alaasar, A. F. Darweesh, Y. Cao, K. Iakoubovskii and M. Yoshio, *J. Mater. Chem. C*, 2024, **12**, 1523–1532.

68 M. Castillo-Vallés, M. Cano, A. Bermejo-Sanz, N. Gimeno and M. B. Ros, *J. Mater. Chem. C*, 2020, **8**, 1998–2007.

69 L. E. Hough, H. T. Jung, D. Krüerke, M. S. Heberling, M. Nakata, C. D. Jones, D. Chen, D. R. Link, J. Zasadzinski, G. Heppke, J. P. Rabe, W. Stocker, E. Körblova, D. M. Walba, M. A. Glaser and N. A. Clark, *Science*, 2009, **325**, 456–460.

70 C. Zhang, N. Diorio, O. D. Lavrentovich and A. Jákli, *Nat. Commun.*, 2014, **5**, 1–6.

71 A. Zep, K. Sitkowska, D. Pociecha and E. Gorecka, *J. Mater. Chem. C*, 2014, **2**, 2323–2327.

72 H. Sasaki, Y. Takanishi, J. Yamamoto and A. Yoshizawa, *J. Phys. Chem. B*, 2015, **119**, 4531–4538.

11308 | *J. Mater. Chem. A*, 2026, **14**, 11294–11309

This journal is © The Royal Society of Chemistry 2026

73 M. R. Tuchband, D. Chen, B. Horanyi, M. Shuai, Y. Shen, E. Korblova, D. M. Walba, N. Kapernaum, F. Giesselmann, M. A. Glaser, J. E. Maclennan and N. A. Clark, *Liq. Cryst.*, 2016, **43**, 1083–1091.

74 *Dispersion and Absorption in Dielectrics I. Alternating Current Characteristics*, The Journal of Chemical Physics, AIP Publishing, https://pubs.aip.org/aip/jcp/article-abstract/9/4/341/218322/Dispersion-and-Absorption-in-Dielectrics-I, accessed on January 21, 2026).

75 *Electrochemical Impedance Spectroscopy in PEM Fuel Cells: Fundamentals and Applications*, ed. X.-Z. Yuan, C. Song, H. Wang and J. Zhang, Springer, London, 2010, pp. 263–345.

76 P. K. Bhowmik, S. L. Chen, H. Han, K. A. Ishak, T. S. Velayutham, U. Bendaoud and A. Martinez-Felipe, *J. Mol. Liq.*, 2022, **365**, 120126.

77 P. K. Bhowmik, S. L. Chen, D. King, H. Han, Z. Bolyard, C. Schmiedl, M. R. Fisch, S. R. Gopal, T. S. Velayutham and A. Martinez-Felipe, *J. Mol. Liq.*, 2024, **398**, 124140.

78 P. K. Bhowmik, O. Noori, S. L. Chen, H. Han, M. R. Fisch, C. M. Robb, A. Variyam and A. Martinez-Felipe, *J. Mol. Liq.*, 2021, **328**, 115370.

79 S. M. Alauddin, N. F. K. Aripin, T. S. Velayutham and A. Martinez-Felipe, *Molecules*, 2020, **25**, 2579.

80 S. Chereddy, P. R. Chinnam, V. Chatare, S. P. Diluzio, M. P. Gobet, S. G. Greenbaum and S. L. Wunder, *Mater. Horiz.*, 2018, **5**, 461–473.

81 C. D. Jones and J. W. Steed, *Chem. Soc. Rev.*, 2016, **45**, 6546–6596.

82 D. B. Amabilino, D. K. Smith and J. W. Steed, *Chem. Soc. Rev.*, 2017, **46**, 2404–2420.

83 M. Liu, G. Ouyang, D. Niu and Y. Sang, *Org. Chem. Front.*, 2018, **5**, 2885–2900.

84 P. R. A. Chivers and D. K. Smith, *Nat. Rev. Mater.*, 2019, **4**, 463–478.

85 N. del Giudice, M. L'Her, E. Scrafton, Y. Atoini, G. Gentile, B. Heinrich, R. Berthiot, A. Aliprandi and L. Douce, *Eur. J. Org Chem.*, 2021, **2021**, 2091–2098.

86 M. Castillo-Vallés, A. Martínez-Bueno, R. Giménez, T. Sierra and M. B. Ros, *J. Mater. Chem. C*, 2019, **7**, 14454–14470.

87 Y. Zhao, Y. Ohm, J. Liao, Y. Luo, H. Y. Cheng, P. Won, P. Roberts, M. R. Carneiro, M. F. Islam, J. H. Ahn, L. M. Walker and C. Majidi, *Nat. Electron.*, 2023, **6**, 206–215.

88 Y. Kim, A. Jeevika, T. Suwa, K. Kubo and K. I. Iimura, *Crystals*, 2024, **14**, 1053.

This journal is © The Royal Society of Chemistry 2026

J. Mater. Chem. A, 2026, **14**, 11294–11309 | **11309**